NDT&E International 150 (2025) 103282

Contents lists available at ScienceDirect

NDT and E International

journal homepage: www.elsevier.com/locate/ndteint

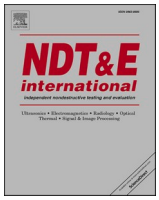

Application of Golay-based total focusing method using a high-frequency, lead-free, flexible ultrasonic array for inspection of thick non-planar industrial components

Elmergue Germano [a,b,*], Morteza Tabatabaeipour [c], Ehsan Mohseni [a], David Lines [a], Charles N. MacLeod [a], Kwok-Ho Lam [b], David Hughes [d], Heather Trodden [d], Anthony Gachagan [a]

[a] University of Strathclyde, 16 Richmond St, Glasgow, G1 1XQ, UK
[b] University of Glasgow, University Avenue, Glasgow, G12 8QQ, UK
[c] Ulster University, 2-24 York Street, Belfast, BT15 1AP, UK
[d] Novosound Ltd, Bo'Ness Rd, Motherwell, ML1 5UH, UK

ARTICLE INFO

Keywords:
High-frequency array
Lead-free
Flexible array
Complex geometry components
Non-planar components
Total focusing method (TFM)
Golay-coded excitation
Ultrasonic NDE

ABSTRACT

The compromise between axial resolution and penetration depth in ultrasound imaging poses a challenge for high-frequency ultrasonic arrays, limiting their ability to effectively inspect thick components in industrial applications. In this work, a commercial 20 MHz, 64 element, 1 mm pitch lead-free flexible linear array was characterised in terms of its performance. The array was subsequently evaluated using Golay-coded excitation techniques to enhance the signal-to-noise ratio (SNR) and operability on non-planar thick components. The SNR improvement verification results were acquired with the array deployed on a 100 mm thick flat aluminium test specimen. As expected, an increase in SNR was observed as the Golay code length increased. The imaging strategy employed a combination of Full Matrix Capture (FMC) and Total Focusing Method (TFM) to assess the performance variations between the conventional pulse excitation and Golay-coded excitation. The Golay-based TFM demonstrated superior performance compared to the conventional pulse-based TFM, with an SNR improvement of 4.95 dB when using the full array aperture to inspect the non-planar steel S355 specimen. A sub-aperture selection approach, based on the effect of the array element beam spread, offered additional SNR improvement of up to 8.2 dB. Greater imaging penetration depth was achieved, with an increase of >40 % compared to conventional pulse-based TFM. Thus, for inspection of thick non-planar industrial components using a lead-free high-frequency array, Golay-coded excitation schemes show excellent potential to enhance SNR, penetration depth and imaging quality.

1. Introduction

High-frequency ultrasonic arrays have gained significant attention in recent years due to their ability to provide images with superior spatial resolution, offering higher sensitivity to small targets in non-destructive testing (NDT) and medical imaging applications [1–3]. In NDT, for instance, these arrays enable the detection of defects in materials or structures at earlier growth stages as compared to lower frequency counterparts. Conversely, high-frequency sound waves have limited penetration depth which can hinder the inspection of thick components.

The growing complexity of industrial components has driven development of conformable ultrasonic probes that enable efficient inspection without the necessity of custom-designed wedges. In line with this development, with considerations for medical contexts, flexible ultrasonic arrays have been investigated for their ability to examine complex and intricate surfaces [4–11]. For instance, the effectiveness of a flexible lead-based 2-D array in inspecting both flat and non-planar test specimens has been demonstrated [4]. Additionally, Full Matrix Capture (FMC) and Total Focusing Method (TFM) imaging strategies with a flexible lead-based linear array have been utilised to detect flaws in planar and complex-geometry aluminium specimens [7]. In FMC, each element of the array sequentially transmits, while all elements simultaneously receive, for each transmission event. In TFM, the beam is focused at every point within the imaging region during both

* Corresponding author. University of Strathclyde, 16 Richmond St, Glasgow, G1 1XQ, UK.
E-mail address: elmergue.germano@strath.ac.uk (E. Germano).

https://doi.org/10.1016/j.ndteint.2024.103282
Received 10 October 2024; Received in revised form 20 November 2024; Accepted 23 November 2024
Available online 25 November 2024

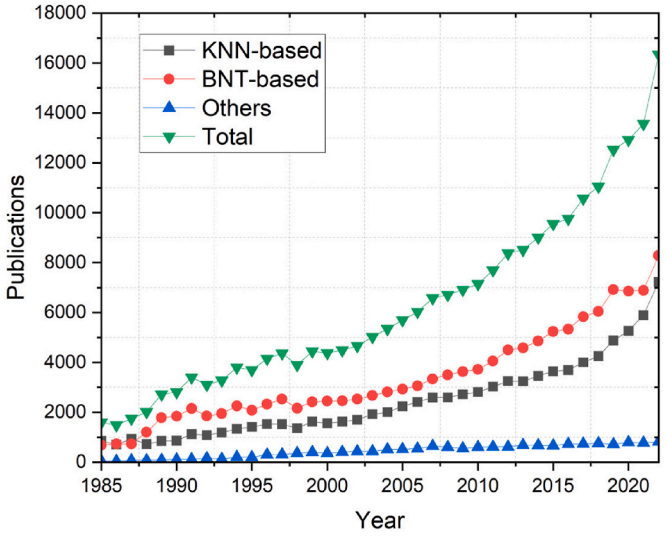

Fig. 1. Annual increase of article publications on various transducer materials from 1985 to 2022, with a particular focus on KNN-based and BNT-based materials, as recorded by the Web of Science platform. A significant rise of over 200 % in published articles between 2004 and 2022 is observed.

transmission and reception stages [7].

Research is ongoing into lead-free alternatives to lead zirconate titanate (PZT), the most widely used piezoelectric material because of its high performance, to comply with the Restriction of Hazardous Substances (RoHS) regulation set by the European Union [12–14] and similar legislations in China and Japan, as well as environmental concerns. Although many promising results of the piezoelectric properties of lead-free materials have been reported over the last two decades, it is still challenging to transfer to large-scale production [15–17]. Achieving optimal ultrasound imaging using lead-free materials continues to pose a persistent challenge, particularly with respect to transducer sensitivity. Fig. 1 shows the annual count of article publications for different transducer materials from 1985 to 2022, as documented by the Web of Science platform, where a >200 % increase in published articles between 2004 and 2022 is evident. Emphasis is placed on potassium sodium niobate (KNN) and sodium bismuth titanate (BNT), with additional materials including barium titanate (BT) and polyvinylidene fluoride (PVDF) also being considered. The data suggests that a notable level of maturity has been achieved in the research within the domain of lead-free piezoceramics over recent years.

The constraints of traditional probe technology in the NDT industry, particularly regarding material composition, flexibility and operational frequency, have driven the development of a new manufacturing approach. This technique enables the production of a high-frequency, lead-free, flexible, linear ultrasonic array, allowing it to adapt to non-planar shapes commonly encountered in nuclear, aerospace, and other industries [18,19]. A pliable metal substrate is the core material of the array. Using vacuum deposition methods, a piezoelectric thin film material is subsequently applied onto it. This enables precise management of thickness, composition, and scalability for large-scale, cost-effective production [20–22]. The practical operation of the array has been showcased [21], in which experiments were undertaken using steel tubing and industrial samples that featured common curvatures encountered in real-world structures.

It is widely known that there is a trade-off between the axial resolution, which is related to the transducer bandwidth, and penetration depth. Short cycle pulses transmit less energy into the medium, which results in good axial resolution but poor penetration. Conversely, longer pulses, containing multiple cycles, provide the opposite effect [23]. Pulse compression techniques can extend the limit associated with this trade-off. Longer coded pulses can be transmitted into the medium and good axial resolution and penetration depth can be achieved by compressing the duration of the received signals through appropriate signal post-processing [23–26]. These techniques have been widely applied for many decades in radar, sonar, medical imaging, and NDT industries. They can be classified based on whether they employ singular or multiple transmissions, and whether their encoding relies on phase or frequency modulation. The prevalent techniques for phase modulation include Golay and Barker codes, while the commonly employed method for frequency modulation is based on chirp signals [23]. For the scope of this study, Golay complementary sequences (GCS) will be exclusively examined, as they minimise anomalous effects from the inverse processing [23].

The benefits of using coded excitation strategies have been demonstrated [27–32]. Higher sensitivity was observed in defect detection when imaging thick carbon fibre reinforced polymer samples with traditional NDT arrays [29]. Moreover, the most common strategies to maintain the signal-to-noise ratio (SNR) in challenging applications are either to reduce the frequency of the ultrasound array or to average the results over multiple transmissions. However, these approaches compromise resolution and acquisition rate, respectively [27]. This paper presents novel work on the combination of coded excitation schemes with high-frequency, lead-free, flexible ultrasonic arrays. This improves the SNR and penetration depth, allowing the inspection of thick components, especially those with intricate surface geometries. The remaining organisational structure of this paper is as follow: Section 2 presents the methodologies of the flexible array characterisation, followed by the inspection study, which included information on the phased-array controller, theoretical information of the phase-modulated Golay-coded excitation and details about the imaging strategy adopted. The experimental results and discussions are detailed in Section 3. The performance of the array was evaluated, comparative analysis in axial resolution at two different frequencies was performed, evaluation of SNR improvement was conducted and TFM imaging comparisons are shown for the conventional pulse excitation as well as the Golay excitation cases. A conclusion of this work is presented in Section 4.

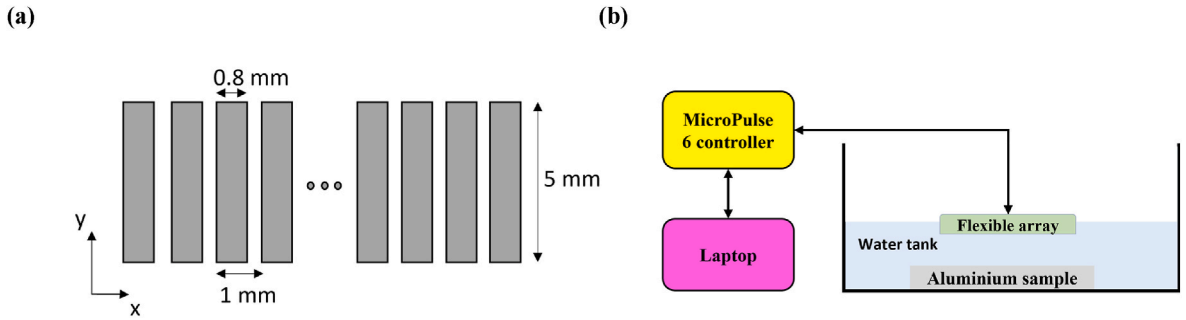

Fig. 2. Flexible array configuration and characterisation configuration. (a) Schematic of the geometry of the array transducers in the x-y plane; (b) Schematic of the conventional pulse-echo setup in a water tank used for array characterisation.

2. Methodology

2.1. Flexible array characterisation

A traditional pulse-echo technique was used to evaluate the performance of a 20 MHz, 64 element, 1 mm pitch flexible linear array (Novosound Ltd., Motherwell, United Kingdom) with overall dimensions of 110 x 30 × 0.5 mm [33]. The schematic diagram of the geometry of the array transducers in the x-y plane is shown in Fig. 2 (a). The experimental setup of the characterisation is depicted in Fig. 2 (b) and included a 6 mm thick flat aluminium plate, which functioned as a reflector, a 3-D printed Polylactic Acid (PLA) transducer holder to allow 4 mm delay line between the array elements and the reflector in a small water tank. The array was connected to a 128/256 MicroPulse 6 controller (Peak NDT, Derby, United Kingdom) using an ipex female to Hypertronics male adapter. The system was controlled by a separate laptop using a Gigabit Ethernet connection. The ArrayGen software platform (Peak NDT, Derby, United Kingdom) was used to define the configuration parameters including the array, sample and the acquisition strategy for transmission and reception. A custom LabVIEW platform was employed for data acquisition.

2.2. Inspection study

2.2.1. Phased array controller

To facilitate the investigation of coded excitation, a programmable ultrasonic research system with tri-level excitation [+V, 0, -V] capability (Vantage 128™, Verasonics Inc., Kirkland, USA) that can generate complex arbitrary waveforms was employed. The Vantage 128™ has a programmable pulser amplitude ranging from 2 to 190 V p-p. The receive frequency range is from 1 to 50 MHz in the high-frequency configuration and an interleaved sampling acquisition scheme was used in this work to achieve an equivalent sampling frequency of 125 MHz [34,35]. The array was connected to the Vantage 128™ using an ipex female to Hypertronics male adapter that interfaced to a universal transducer adapter (UTA) 160-DH/32 LEMO. The acquisition data flow occurs from the array to the host memory of the computer. The signals are sampled and digitised in 14-bit analogue to digital converters. It is then conditioned in the digital front end, with two digital filters and decimators provide low-pass or band-pass filtering. The signal is locally stored and is subsequently transferred to the host memory via peripheral component interconnect express (PCIe) cables [34,35].

2.2.2. Golay-coded excitation

Golay complementary sequences (GCS) belong to a subset of binary code pairs found in a larger collection of signals referred to as complementary pairs. These sequences encompass two codes with the same length, $L = 2^n$ cycles, where n represents an integer with a minimum value of 1. Their auto-correlation functions exhibit side-lobes of equivalent magnitudes but opposite polarities. Adding them together yields a combined auto-correlation function featuring zero side lobes [23,27,36]. The sequence, or code, is transmitted to a transducer, and a decoding filter is applied during the reception phase. The received data is compressed through cross-correlation, using a matched filter derived from the initial excitation pulse. The summation is then performed on the pair of cross-correlated signals.

Sets of GCS were constructed using a recursive method. The approach involves starting with two shorter sequences that are subsequently combined through a prescribed method to create longer sequences. Consider the variables $a(k)$ and $b(k)$ as the elements $(k = 0, 1, 2, 3, \ldots, 2^n - 1)$ of two complementary codes of length 2^n, with the elements equal to either $+1$ or -1

$$a_0(k) = \delta(k) \tag{1}$$

$$b_0(k) = \delta(k) \tag{2}$$

Table 1
Golay complementary sequences with different lengths.

Length ($L = 2^n$)	n	Sequence A	Sequence B
2	1	[1, 1]	[1, −1]
4	2	[1, 1, 1, −1]	[1, 1, −1, 1]
8	3	[1, 1, 1, −1, 1, 1, −1, 1]	[1, 1, 1, −1, −1, −1, 1, −1]
16	4	[1, 1, 1, −1, 1, 1, −1, 1, 1, 1, 1, −1, −1, −1, 1, −1]	[1, 1, 1, −1, 1, 1, 1, −1, 1, −1, −1, −1, 1, 1, 1, −1]
32	5	[1, 1, 1, −1, 1, 1, −1, 1, 1, 1, 1, −1, −1, −1, 1, −1, 1, 1, 1, −1, 1, 1, −1, 1, −1, −1, −1, 1, 1, 1, −1, 1]	[1, 1, 1, −1, 1, 1, −1, 1, 1, 1, 1, −1, −1, −1, 1, −1, −1, −1, −1, 1, 1, −1, −1, 1, −1, 1, 1, 1, 1, −1, −1, −1, 1, −1]

$$a_n(k) = a_{n-1}(k) + b_{n-1}\left(k - 2^{n-1}\right) \tag{3}$$

$$b_n(k) = a_{n-1}(k) - b_{n-1}\left(k - 2^{n-1}\right) \tag{4}$$

where $\delta(k)$ is the Kronecker delta function. In the case where $n = 1$, the variable k assumes values of 0 and 1. Solving equations (1)–(4) results in the complementary sequences $A = [1, 1]$ and $B = [1, -1]$. Longer sequences can now be created. Another Golay pair of length twice that of the pair A and B can be formed by concatenation [AB, A(-B)]. For example, when $n = 2$, the complementary sequences become $A = [1, 1, 1, -1]$ and $B = [1, 1, -1, 1]$. Executing these operations iteratively enables the generation of more extended sequences. Table 1 displays GCS with lengths up to 32. A compromise for achieving optimal range of side lobe cancellation is the necessity for two consecutive firings, thereby introducing motion-dependent decoding errors [23,37].

Instead of employing direct transmission, the established technique for integrating binary coded excitation encompasses modulation with a waveform [23,38]. Thus, Golay-coded pulse trains were programmed in the Vantage 128™ and modulated with a waveform at 20 MHz. The resulting waveforms were utilised to excite the array and for data acquisition.

A simulation using the Verasonics Vantage software was employed to demonstrate the principle of side lobe cancellation. The ultrasonic array was positioned on an acoustic medium (longitudinal velocity of 6320 m/s) with only a single target. An illustration of the imaging plane is shown in Fig. 3 (a). It highlights the location of the array elements and the target. The excitation employed a single cycle, used for reference, and 4 cycles of Golay waveforms, as depicted in Fig. 3(b)–(d), with all signals in tri-level representation as defined by the instrumentation. The green arrows for the Golay case indicates the phase of the complementary sequences of length 4. Full matrix acquisition was simulated and random noise was deliberately introduced to the received signals. The response of a single cycle is depicted in Fig. 3 (e). For the Golay case, the received signals undergo compression via convolution, employing a matched filter generated from the excitation pulse, as shown in Fig. 3 (f). The A-scan of interest is derived from the summation of the pair of convolved signals, as depicted in Fig. 3 (g).

2.2.3. Full matrix capture and total focusing method

To implement the CGS, two transmissions are required. A MATLAB-based platform was developed to interface with the Vantage 128™ and allow FMC acquisition. In FMC, each array element transmits in turn and all array elements receive on each transmission event. This allows all possible transmit-receive combinations to produce a complete set of A-scans. For each transmission, the dataset contains $N \times N$ matrix of A-scans, where N is the number of elements in the array. The primary limitation of the FMC method is the reduced acoustic power output from individual elements during transmission. This leads to a decrease in SNR for each transmit-receive pair compared to conventional multi-element aperture imaging techniques [36,39]. The data was stored in a MAT-file format, and subsequently processed in MATLAB. Following data collection, the principle of side lobe cancellation, where the pair of Rx

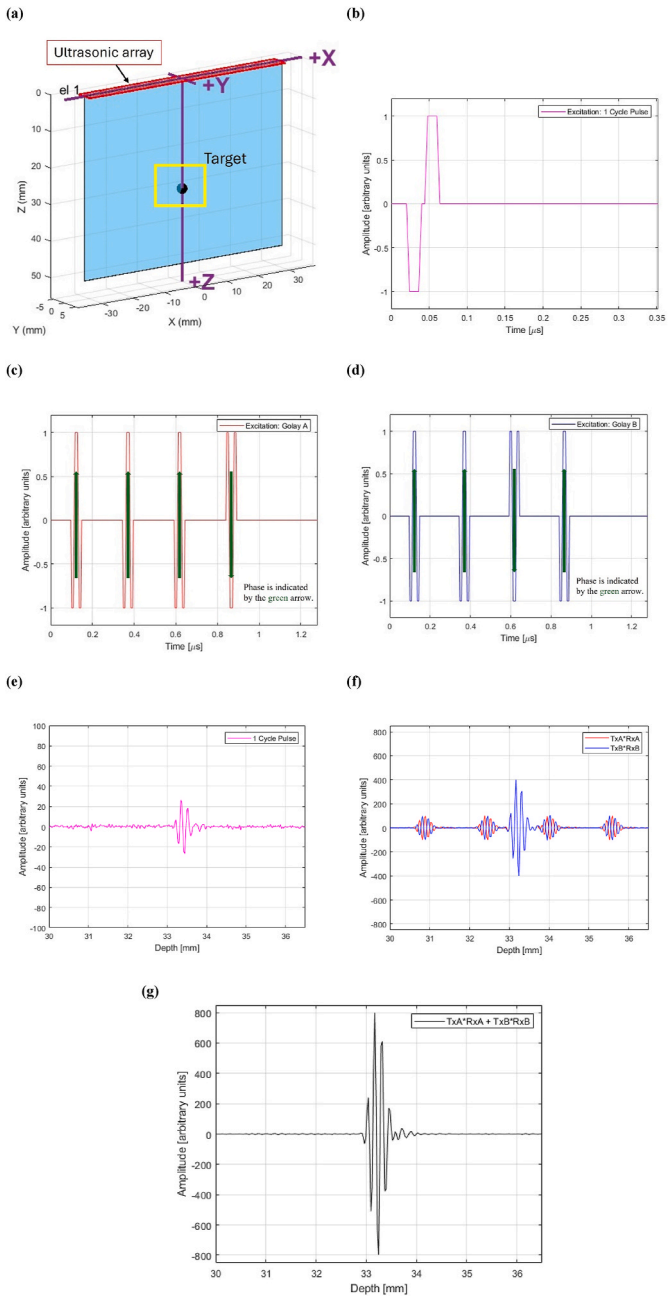

Fig. 3. Simulation work to demonstrate the side lobe cancellation principle. (a) Illustration of the imaging plane showcasing the array with emphasis on the position of its elements and the target location. (b) Single cycle excitation waveform (tri-level representation) utilised as reference. (c) Golay A excitation waveform (tri-level representation). (d) Golay B excitation waveform (tri-level representation). (e) Response of the single cycle excitation. (f) and (g) Demonstration of the principle of side lobe cancellation using the pair of complementary Golay sequences (Golay A and Golay B) of 4 cycles. The convolution operator is represented by the "*" symbol. TxA and TxB are the transmit signals in Fig. 3 (c) and 3 (d), respectively. RxA and RxB are the receive signals A and B, respectively.

signals are converted to a single A-scan and where the sidelobes from the pair are removed, was applied and the resulting decoded signal was further processed with a TFM imaging algorithm. In TFM, the beam is focused at each point within the image region on both transmit and receive. This region is initially discretised into a grid. Each point in the grid is estimated by summing the path-compensated amplitudes over the set of transmit-receive pairs, hence, producing a focus at each point

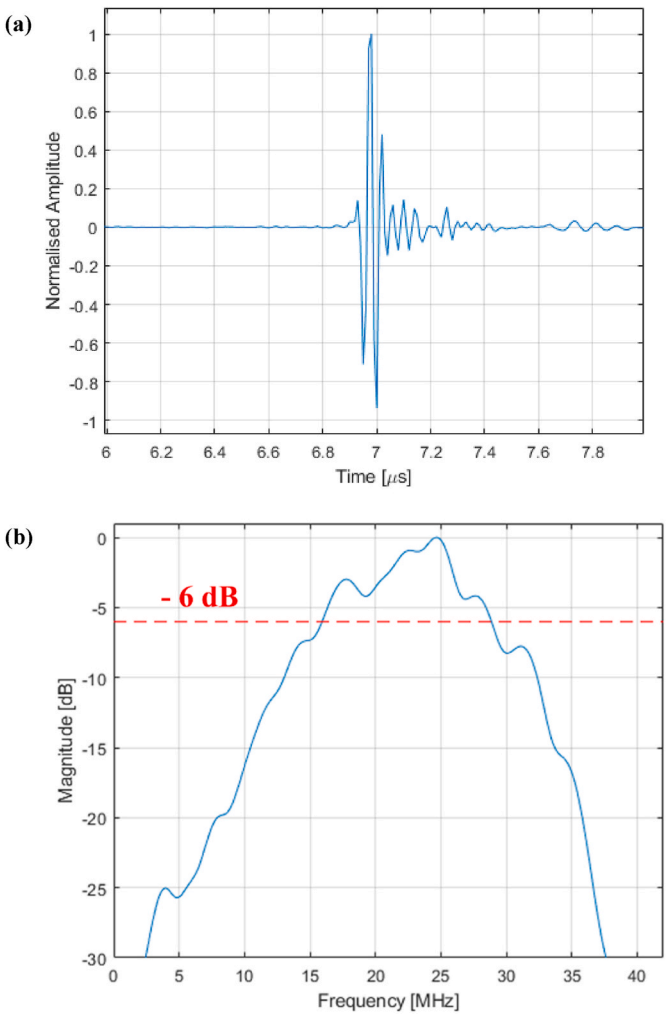

Fig. 4. Pulse-echo response of the array. (a) Time-domain response and (b) corresponding frequency spectrum from the front wall reflection of the aluminium test specimen. The schematic of the data acquisition setup is shown in Fig. 2 (b).

[39].

3. Experimental results and discussions

3.1. Flexible array characterisation

The array was excited with a 24 ns 80 V p-p electrical pulse, generated by the MicroPulse 6 controller, as depicted in Fig. 2 (b), which was the closest the software permitted to the ideal 25 ns for 20 MHz. The custom LabVIEW platform is set to acquire FMC data, which was subsequently stored in a HDF5 Multi-Frame Matrix Capture (MFMC) file format [40]. Data was then processed using MATLAB and the FMC diagonal, representing each element pulse-echo response, was examined. Fig. 4 represents the average measured pulse-echo response of the array from the front face of the reflector, indicating the typical response of the array. The frequency spectrum was obtained from the individual time-domain waveforms using the Fast Fourier Transform (FFT) method and then averaged. The average peak frequency and the −6 dB bandwidth were determined, with the average of all the peak frequencies (measured from 64 A-scans of the matrix diagonal) determined to be 24.12 MHz, with a standard deviation of 1.82 MHz, and the average −6 dB bandwidth calculated to be 64.9 %. Notably, this novel lead-free, flexible array complies with the BS EN ISO 18563–2:2017 standard [33].

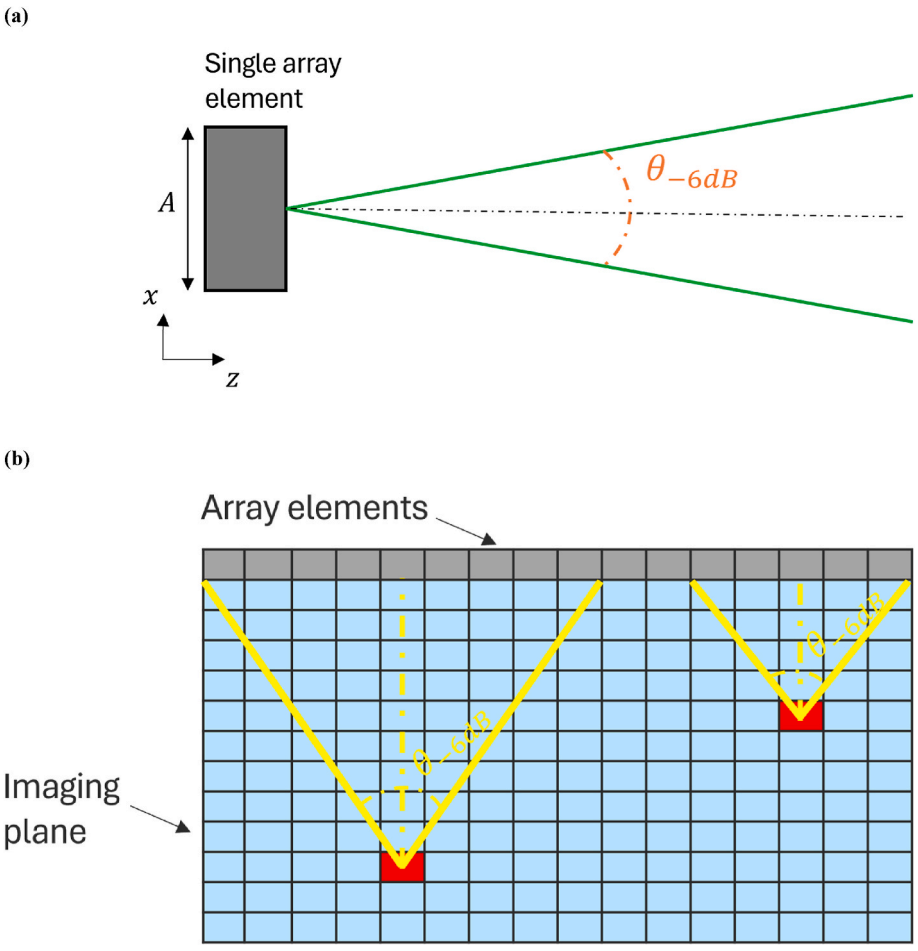

Fig. 5. Beam spread analysis. (a) Single array element schematic with emphasis of the beam spread angle. (b) Principle of sub-aperture selection based on the beam spread or element directivity analysis. The element size is 0.8 mm.

3.2. Inspection study

3.2.1. Resolution

Next, the theoretical improvement in axial resolution offered by high-frequency ultrasonic waves was examined. The performance of a 5 MHz, 64 element, 1 mm pitch flexible linear array was evaluated against the 20 MHz 64 element 1 mm pitch lead-free flexible linear array. The arrays were in direct contact with a 300 x 20 × 100 mm planar aluminium test specimen through EchoPure ™ couplant gel (Echo Ultrasonics®, LLC, Bellingham, USA). In TFM imaging, it is usual to include A-scan contributions from all element pairs for each pixel. However, it is essential to ensure that the directivity of each element is wide enough for the A-scan to contribute usefully to the signal, rather than simply adding noise. This is particularly important when imaging close to the array, but applies more widely when performing TFM where the pitch of the array is greater than the conventional $\lambda/2$ criterion [39]. One approach, that addresses this issue, is to mask contributions from elements where the path of the ray exceeds a specified angle with respect to the normal to the element. This threshold angle would typically be derived from the element directivity angle [41–43]. Therefore, by considering the predicted array element beam spread angle (or directivity angle), a sub-aperture imaging configuration can be determined for each array experimental set-up and subsequently employed to improve SNR. Fig. 5 (a) shows a schematic of a single array element, highlighting the beam spread angle for the arbitrarily selected threshold of −6 dB with respect to the maximum at that range. This angle consists of the total angular extent measured from one side to the other of the main lobe of the ultrasound beam in the far field. A beam computation model of an unfocused longitudinal transmission was produced using the NDT simulation software package CIVA [44] for the 20 MHz array case. Beam computation models using CIVA have previously been employed for weld inspection applications [45]. Hence, the beam spread angle (-6 dB) obtained from a representative single array element model is 22.63°. This compares favourably with the theoretical value of 23.43° calculated using Eq. (7) [46].

$$\theta_{-6dB} = 2\sin^{-1}(0.514\lambda / A) \tag{7}$$

where λ is the wavelength in the specimen and A is the aperture of the transducer. The −6 dB width can then be obtained by applying trigonometry principles at the desired imaging depth in the sample (z-axis). For example, at the depth corresponding to the location of the second target (17 mm), the −6 dB width is 7.05 mm, thus, an 8-element sub-aperture was employed. This the sub-aperture selection methodology is illustrated in Fig. 5 (b).

Fig. 6 (a) shows the schematic of the acquisition setup. A 64 g PLA block was positioned on the array elements to ensure uniform pressure, thus facilitating consistent signal acquisition. The test specimen featured four side-drilled holes (SDHs) machined from the side, each with a diameter of 1 mm and a length of 20 mm. The SDHs were positioned 8–17 mm into the sample with the centres spaced 3 mm apart along the axial direction. The Vantage 128™ was used to acquire FMC dataset. The arrays were excited using half a cycle at 80 V, with the receive gain set to 40 dB. Fig. 6 (b) and (d) depict TFM images formed using the 5 MHz array (using a 48-element sub-aperture, by considering the beam spread effect) and the 20 MHz array (employing an 8-element sub-

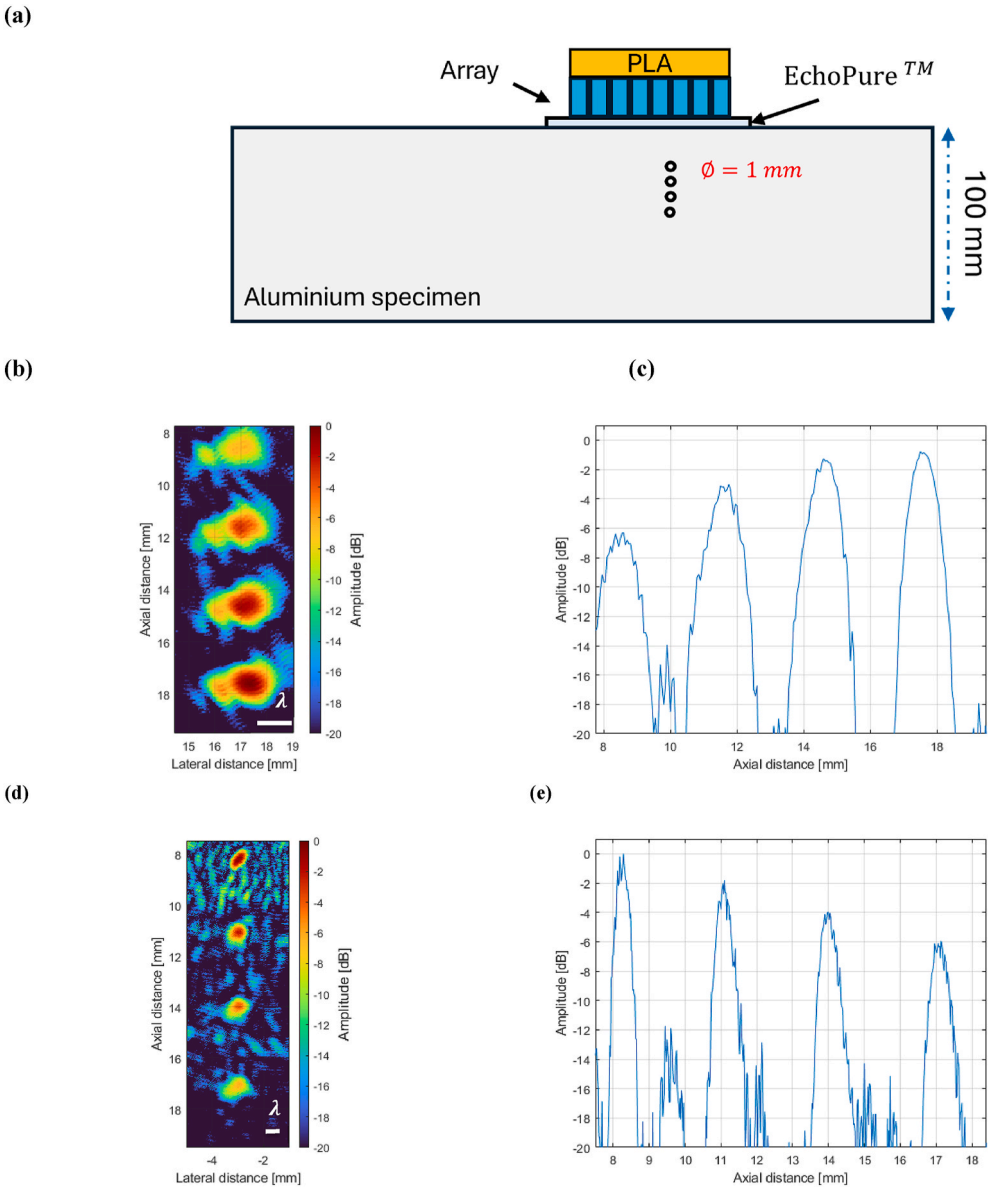

Fig. 6. Axial resolution evaluation. (a) Schematic of the axial resolution setup. The 5 MHz and the 20 MHz arrays were directly coupled to the aluminium specimen in turn. A PLA block (64 g) was placed on top of the array elements to ensure alignment; (b) TFM image corresponding to the 5 MHz array using a 48-element sub-aperture; (c) Cross-section of the TFM image of the 5 MHz array through the central axis of the SDHs; (d) TFM image corresponding to the 20 MHz array using an 8-element sub-aperture; (e) Cross-section of the TFM image of the 20 MHz array through the central axis of the SDHs. The element size of each array is 0.8 mm. The pattern observed in the cross-section of the TFM images arises as a consequence of the sub-aperture selection.

aperture), respectively. The SNR for each target is higher for the 5 MHz, with a maximum value of 24.8 dB, compared to the 20 MHz array, which achieved a maximum value of 18.6 dB. The observed increase in SNR at 5 MHz is consistent with expectations, attributed to the material properties of the transducer, larger aperture and the resultant higher transmission energy. As anticipated, the 20 MHz array demonstrated higher axial resolution compared to the 5 MHz array. The SDHs can be clearly distinguished along the axial direction for the 20 MHz case, as shown in Fig. 6 (e). In contrast, in the 5 MHz case, shown in Fig. 6 (b), as expected from the lower operating frequency, the SDHs are less well resolved and it would be challenging to separate them at 5 MHz if the holes were positioned any closer.

3.2.2. *Evaluation of SNR improvement*

This experimental study aimed to verify improvement in SNR experimentally as the length of the Golay codes increased. Golay-coded excitations comprising of 2, 4 and 8 cycles were used. The 20 MHz array was directly coupled to the 100 mm thick flat aluminium sample (as depicted in Fig. 6) using EchoPure ^{TM} couplant gel. In this case, the target was an SDH with a 1.5 mm diameter, located at a 30 mm depth from the top surface of the sample. To ensure consistent pressure is being employed on the array, a PLA block (64 g) was placed on top of the array elements. The Verasonics Vantage 128™ was operated to acquire FMC data. The array was excited with an excitation voltage of 60 V and the receive gain was set to 40 dB. The beam spread effect was considered and a sub-aperture of 14 elements was utilised. TFM images were subsequently produced and Equation (6) [47] was used to quantify the SNR. Given the known locations of defects, the SNR value was computed within a specified region surrounding each defect. Moreover, the noise level was determined as the RMS of the image noise, excluding any indication of defects [47].

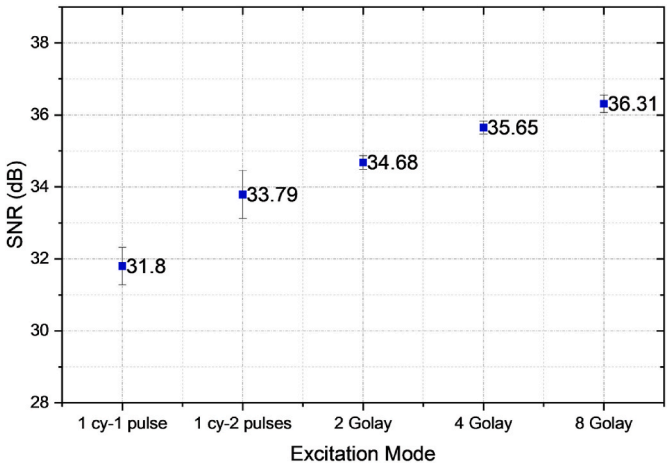

Fig. 7. Measured SNR with respect to different excitation modes. Enhancement in SNR noted with increase in the length of the Golay codes. The term "1 cy-1 pulse" indicates one cycle with a single pulse, while "1 cy-2 pulses" indicates one cycle with two pulses.

$$SNR = 20\ log_{10}\left(\frac{A_{max}(r)}{\sqrt{(A_{noise}(I_n)^2)}}\right) \tag{6}$$

The SNR of the echo was evaluated across a series of acquisition modes, commencing with the reference point of single-cycle excitation. The second instance used the same setup but with a two-pulse excitation. Subsequent modes involved Golay acquisition and processing for 2, 4, and 8 cycles each in sequence. Fig. 7 shows the measured SNR for the different excitation modes. As anticipated, improvement in SNR was observed as the length of the Golay codes increased. It should be noted that extending the length of the transmitting signals results in an increased dead zone before the detection of the first receive signals. Therefore, selection of the appropriate Golay length relies on the specific application and will be a compromise between acceptable SNR and ensuring that the length of the dead zone does not compromise the near-surface defect detection performance [27].

3.2.3. Imaging a non-planar component

The aim of this study was to evaluate the improvement in SNR on a non-planar component using the designed Golay complementary sequences to excite the lead-free array. An imaging comparison is presented in terms of the Golay-based TFM and the conventional pulse-based TFM. Experimental work was conducted on a 150 x 20 × 70 mm non-planar steel S355 specimen with a radius of curvature of 150 mm to represent non-planar industrial components. The specimen is depicted in Fig. 8 and has machined defects, which consist of three SDHs, 2 mm in diameter, 20 mm long, drilled from the side of the sample. The SDHs are positioned 15 mm apart from each other laterally and 10 mm apart axially.

Pulse-echo measurements were conducted using the 20-MHz, lead-free, flexible ultrasonic array. The array was in direct contact with the sample using EchoPure ^{TM} couplant gel. It was magnetically attached to the sample by means of two 10 mm diameter, 5 mm thick neodymium magnetic discs. The key acquisition parameters of the experimental setup included 80 V for excitation, a receive gain of 40 dB and the sample rate set to 125 MHz. A single cycle was initially used to excite the array and produce the conventional pulse-based TFM image. Then, in the context of this particular application, where the positions of the defects are known, and considering the enhancement in SNR as well as the impact of the dead zone, 8 cycles of Golay excitation were employed to excite the array and the Golay-based TFM image was produced. Fig. 9 shows TFM images utilising all 64 array elements during FMC data acquisition for both scenarios corresponding to the region of interest. To assess the enhancement in image quality, the SNR was quantified using Equation (6). Table 2 shows the measured SNR values from each TFM image depicted in Fig. 9. Fig. 9 (a) and (b) show SDH1 being detected for both excitation cases, with an improvement of 4.95 dB calculated for the Golay result when compared to the conventional pulse excitation. Transmitting 8 cycles of Golay sequences allowed deeper penetration into the sample, as shown in Fig. 9 (d), enabling SDH2 to be detected, with an SNR of 16.28 dB. The targets in Fig. 9(c)–(e) and (f) were not detected.

3.2.4. Effect of the element directivity

It has been noted (in sub-section 3.2.1.) that in TFM imaging, it is standard practice to incorporate A-scan contributions from all possible element pairs for each pixel. This can introduce unnecessary noise if the directivity of each element is not wide enough for the A-scan to contribute meaningfully to the signal. Hence, by accounting for the beam spread angle of the array element, a sub-aperture from the initial FMC dataset can be selected, resulting in an improved SNR. Fig. 10 depicts the TFM images employing a 6-element sub-aperture for the SHD1 region, a 12-element sub-aperture for the SHD2 region and a 16-element sub-aperture for the SDH3 region. SDH1 and SDH2 were detected in both excitation scenarios, as depicted in Fig. 10(a)–(d). The selected sub-aperture, leveraging the element directivity effect, enable the detection of SDH2 in the pulse excitation case, as shown in Fig. 10 (c), which was otherwise undetectable with all 64 array elements. The Golay case also detected SDH2, with an SNR improvement of 2.74 dB.

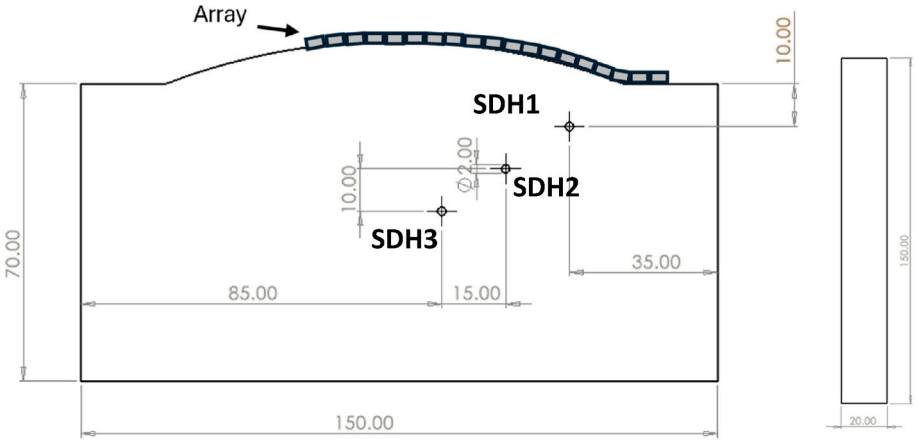

Fig. 8. Schematics of the steel S355 sample displaying the arrangement of side-drilled holes at various depths. Bottom view is depicted on the right. All dimensions are in millimeters (mm).

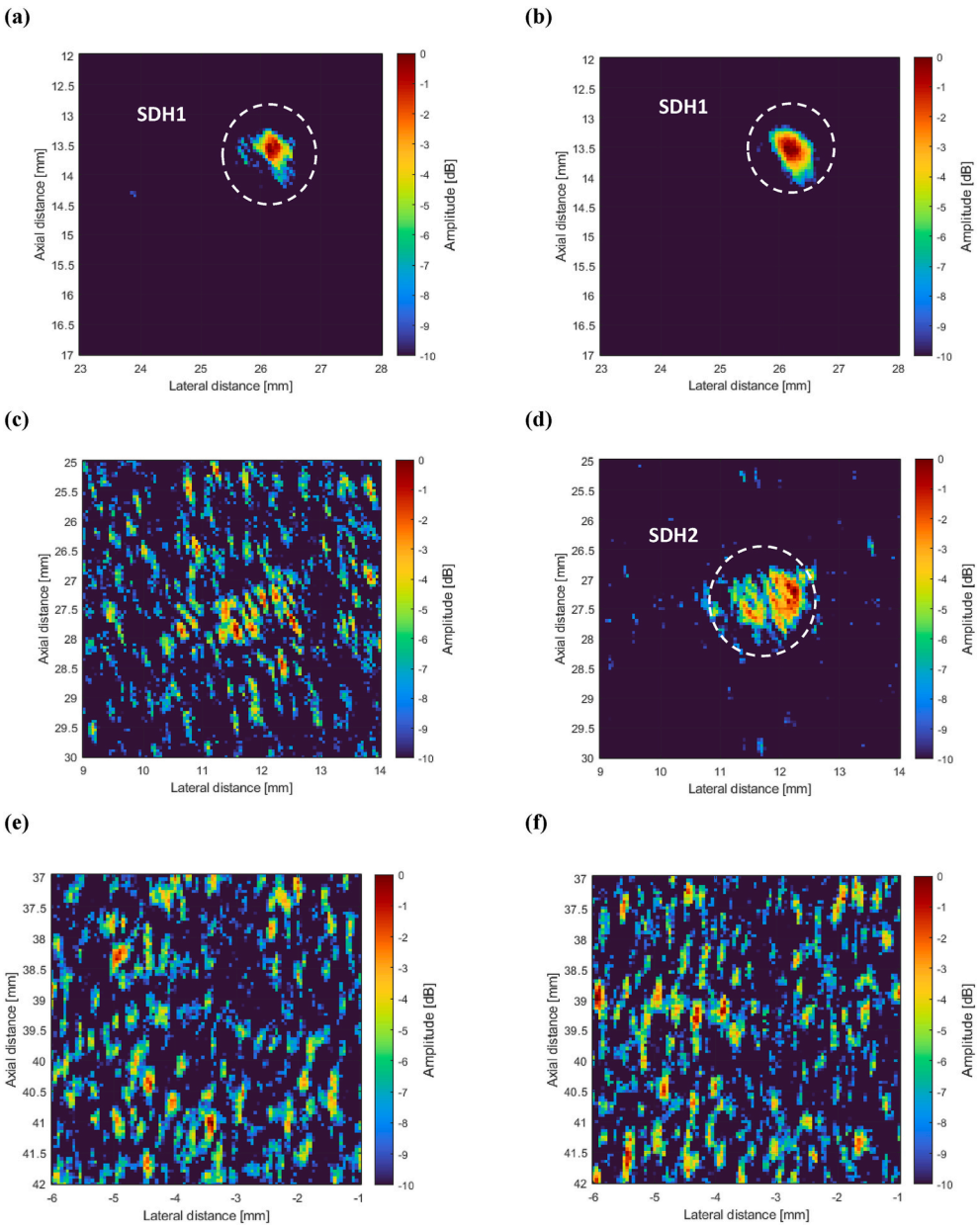

Fig. 9. TFM images employing all 64 elements for FMC data acquisition (a) Conventional pulse-based TFM image for SDH1; (b) Golay-based TFM for SDH1; (c) conventional pulse-based TFM image for SDH2; (d) Golay-based TFM for SDH2; (e) conventional pulse-based TFM image for SDH3; (f) Golay-based TFM for SDH3; Golay-based TFM exhibits superior imaging contrast and higher SNR compared to the conventional pulse-based TFM, indicating improvement in imaging quality.

Table 2
SNR measurement from TFM images using all 64 elements. Golay-coded excitation offers improved detection capability with higher SNR.

Targets	SNR (dB)		Improvement
	Pulse	Golay	
SDH1	19.57	24.52	4.95 dB
SDH2	Not detected	16.28	Detection
SDH3	Not detected	Not detected	Not detected

Importantly, the detection of SDH3 was now successfully achieved in the Golay case, as illustrated in Fig. 10 (f), whereas the pulse excitation case did not detect SDH3 (Fig. 10 (e)). Table 3 displays the measured SNR values corresponding to each TFM image depicted in Fig. 10. The element directivity effect resulted in further SNR improvement overall. For the Golay case, 8.2 dB of SNR improvement was observed for the SDH2. For all cases, improvement in imaging quality was obtained. The Golay-based TFM outperforms the conventional pulse-based TFM. Improved imaging penetration depth using a combination of a lead-free, flexible ultrasonic array with coded excitation strategies has been demonstrated.

4. Conclusion

In this work, a 20-MHz, lead-free, flexible ultrasonic array has been characterised. The array complies with the BS EN ISO 18563–2:2017 standard, with an average −6 dB bandwidth of 60.6 %. Golay-coded excitation schemes have been designed and implemented to overcome the limit associated to the axial resolution and penetration depth trade-off. An improvement verification study has been conducted and as expected, increase in SNR was observed as the length of Golay codes increased. The appropriate length of the Golay codes depends on specific

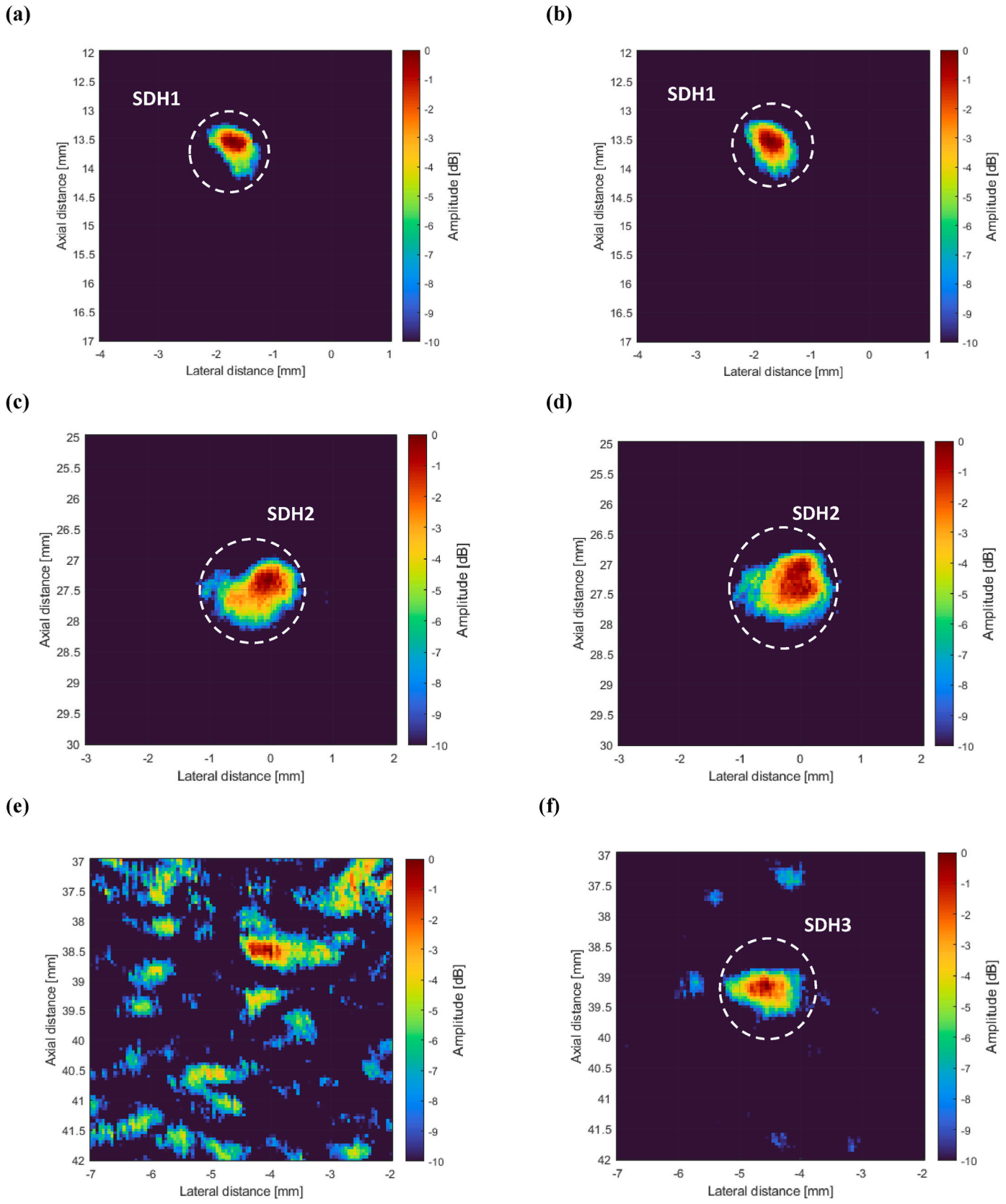

Fig. 10. TFM images employing different sub-aperture considering the beam spread effect. (a) Pulse-based TFM image for SDH1; (b) Golay-based TFM for SDH1; (c) Pulse-based TFM image for SDH2; (d) Golay-based TFM for SDH2; (e) Pulse-based TFM image for SDH3. An unacceptable noise level observed; (f) Golay-based TFM for SDH3. Improved imaging depth observed.

Table 3
SNR measurement from the TFM images in Fig. 10. The selected sub-aperture, exploiting the element directivity effect offered enhanced detection capability for both the pulse and the phase-modulated Golay excitation cases.

Targets	SNR (dB)		Improvement
	Pulse	Golay	
SDH1	23.16	24.67	1.51 dB
SDH2	21.74	24.48	2.74 dB
SDH3	Not detected	17.15	Detection

application, including acceptable SNR as well as the dead zone not compromising the near-field defect detection performance. The FMC technique for acquisition and the TFM algorithm for imaging were employed to compare the performance of the conventional pulse excitation against Golay-coded excitation strategies. Using the full-array aperture and in direct contact to a non-planar steel S355 test specimen, the Golay-based TFM outperformed the conventional pulse-based TFM, with 4.95 dB of SNR improvement observed. The selected sub-apertures based on the beam spread effect provided further SNR improvement (>8 dB) and greater imaging penetration depth was achieved, surpassing the conventional approach by more than 40 %, successfully detecting SDH3 with an SNR of 17.15 dB, which was undetectable under the conventional excitation condition. The approach described in this work, integrating a high-frequency lead-free flexible ultrasonic array with Golay-coded excitation, holds promise for improving the SNR, penetration depth and imaging quality for the inspection of thick section components with a complex surface profile. Future research will focus on further enhancing the performance of the 20-MHz, lead-free, flexible ultrasonic array by exploring frequency and phase modulated signals beyond the phase modulated Golay excitation signals. Another avenue for future work involves expanding the application of the developed approach to diverse industrial scenarios. This includes testing this development on a wider range of materials and component geometries to evaluate its robustness and versatility. The development of real-time data acquisition and processing algorithms will also be pursued to facilitate inspections and improve the practicality of the technology for industrial applications.

CRediT authorship contribution statement

Elmergue Germano: Writing – review & editing, Writing – original draft, Visualization, Software, Methodology, Investigation, Formal analysis, Data curation, Conceptualization. **Morteza Tabatabaeipour:** Writing – review & editing, Visualization, Software, Methodology, Formal analysis. **Ehsan Mohseni:** Writing – review & editing, Supervision, Resources, Project administration, Investigation, Conceptualization, Validation. **David Lines:** Writing – review & editing, Supervision, Software, Methodology, Conceptualization, Validation. **Charles N. MacLeod:** Resources. **Kwok-Ho Lam:** Writing – review & editing, Supervision, Resources, Project administration, Methodology. **David Hughes:** Writing – review & editing, Supervision, Resources, Project administration, Conceptualization. **Heather Trodden:** Resources, Project administration. **Anthony Gachagan:** Writing – review & editing, Supervision, Resources, Project administration, Methodology, Funding acquisition, Conceptualization, Validation.

Declaration of competing interest

The authors declare that they have no known competing financial interests or personal relationships that could have appeared to influence the work reported in this paper.

Data availability

Data will be made available on request.

References

[1] Mohammadkhani R, Zanotti LF, Padiyar M J, Petrunin I, Raposo J, Tsourdos A, Gray I. Improving depth resolution of ultrasonic phased array imaging to inspect aerospace composite structures. Sensors Jan. 2020;20:1–18. https://doi.org/10.3390/s20020559.

[2] Wong CM, Chan SF, Liu R, Zhang J, Wu WC, Liang Z, Yau HM, Wang DY, Li S, Lam KH, Qiu WB, Luo HS, Dai JY. 20-MHz phased array ultrasound transducer for in vivo ultrasound imaging of small animals. Ultrasonics Dec. 2022;126:1–9. https://doi.org/10.1016/j.ultras.2022.106821.

[3] Ninghao W, Xinze L, Jie X, Yang J, Yaoyao C, Xiaohua J. A high frequency endoscopic ultrasound imaging method combining chirp coded excitation and compressed sensing. Ultrasonics 2022;121:1–11. https://doi.org/10.1016/j.ultras.2021.106669.

[4] Hu H, Zhu X, Wang C, Zhang L, Li X, Lee S, Huang Z, Chen R, Chen Z, Wang C, Gu Y, Chen Y, Lei Y, Zhang T, Kim N, Guo Y, Teng Y, Zhou W, Li Y, Nomoto A, Sternini S, Zhou Q, Pharr M, di Scalea FL, Xu S. Stretchable ultrasonic transducer arrays for three-dimensional imaging on complex surfaces. Sci Adv Mar. 2018;4(3):1–11. https://doi.org/10.1126/sciadv.aar3979.

[5] Lane CJL. The inspection of curved components using flexible ultrasonic arrays and shape sensing fibres. Case Stud. Nondestruct. Test. Eval. 2014;1:13–8. https://doi.org/10.1016/j.csndt.2014.03.003.

[6] Zheng Y, Zhao X, Song S-J, Zhang J. Beam generating and sound field modeling of flexible phased arrays for inspecting complex geometric components. Wave Motion 2020;94. https://doi.org/10.1016/j.wavemoti.2019.102494.

[7] Nakahata K, Tokumasu S, Sakai A, Iwata Y, Ohira K, Ogura Y. Ultrasonic imaging using signal post-processing for a flexible array transducer. NDT&E International 2016;82:13–25. https://doi.org/10.1016/j.ndteint.2016.04.002.

[8] Wang C, Chen X, Wang L, Makihata M, Liu HC, Zhou T, Zhao X. Bioadhesive ultrasound for long-term continuous imaging of diverse organs, vol. 377. The American Association for the Advancement of Science; 2022. p. 517–23. https://doi.org/10.1126/science.abo2542.

[9] Elloian J, Jadwiszczak J, Arslan V, Sherman JD, Kessler DO, Shepard KL. Flexible ultrasound transceiver array for non-invasive surface-conformable imaging enabled by geometric phase correction, vol. 12. Nature Publishing Group; 2022. p. 1–12. https://doi.org/10.1038/s41598-022-20721-7.

[10] Chang J, Chen Z, Huang Y, Li Y, Zeng X, Lu C. Flexible ultrasonic array for breast-cancer diagnosis based on a self-shape-estimation algorithm. Ultrasonics 2020;108. https://doi.org/10.1016/j.ultras.2020.106199.

[11] Roy O, Mahaut S, Casula O. Control of the ultrasonic beam transmitted through an irregular profile using a smart flexible transducer: modelling and application. Ultrasonics 2002;40:243–6. https://doi.org/10.1016/S0041-624X(02)00145-2.

[12] European Directive 2002/95/EC. Restriction of the use of certain hazardous substances in electrical and electronic equipment. Off J Eur Union Feb. 2003;L37:19–23.

[13] European Directive 2011/65/EU. Restriction of the use of certain hazardous substances in electrical and electronic equipment. Off J Eur Union Jul. 2011;L174:88–110.

[14] European Directive 2018/736/EU. Restriction of the use of certain hazardous substances in electrical and electronic equipment. Off J Eur Union May 2018;L123:94–6.

[15] Ringgaard E, Levassort F, Wang K, Vaitekunas J, Nagata H. Lead-free piezoelectric transducers. IEEE Jan. 2024;71(1):3–15. https://doi.org/10.1109/TUFFC.2023.3340950.

[16] Koruza J, Bell AJ, Frömling T, Webber KG, Wang K, Rödel J. Requirements for the transfer of lead-free piezoceramics into application. J Materiomics Mar. 2018;4(1):13–26. https://doi.org/10.1016/j.jmat.2018.02.001.

[17] Rödel J, Webber KG, Dittmera R, Jo W, Kimura M, Damjanovic D. Transferring lead-free piezoelectric ceramics into application. J Eur Ceram Soc Jun. 2015;35(6):1659–81. https://doi.org/10.1016/j.jeurceramsoc.2014.12.013.

[18] Hughes D, Irving D. Ultrasound array transducer manufacturing. United Kingdom patent WO2019166815 (A1). Sep.6, 2019.

[19] Hughes D, Gibson D, Irving D. Formation of piezoelectric Devices. Sep. 6, 2019. United Kingdom Patent WO2019166805 (A2).

[20] Pelayo Garcia M, Gibson D, Hughes DA, Garcia Nuñez C. A refined quasi-static method for precise determination of piezoelectric coefficient of nanostructured standard and inclined thin films. Advanced Physics Research Nov. 2023:1–12. https://doi.org/10.1002/apxr.202300091.

[21] Rocks B, Gaudenzi F, Irving D, Hughes DA. Fully-flexible thin-film ultrasonic array for use in industrial NDE applications. Glasgow, Scotland: IEEE International Ultrasonics Symposium; 2019.

[22] Rocks B, Irving D, McAughey KL, Wells HG, Thring CB, Hughes DA. Noise reduction in flexible-array-inspection images with machine learning for aerospace applications. In: Proceedings of the 2021 IEEE international ultrasonics symposium (IUS); September 2021. p. 11–6. Xi'an, China.

[23] Chiao RY, Hao X. Coded excitation for diagnostic ultrasound: a system developer's perspective. Tran. Ult. Feb. 2005;52(2):160–70. https://doi.org/10.1109/TUFFC.2005.1406543.

[24] Gini F, De Maio A, Patton L. Classical radar waveform design. In: Waveform design and diversity for advanced radar systems. London, England, United Kingdom: The Institution of Engineering and Technology; 2012. p. 1–9.

[25] Levanon N, Mozeson E. Matched filter. In: Radar signals. Hoboken, New Jersey, USA: John Wiley & Sons; 2004. p. 20–4.

[26] Isla J, Cegla F. Coded excitation for pulse-echo systems. IEEE Apr. 2017;64(4):736–48. https://doi.org/10.1109/TUFFC.2017.2661383.

[27] Lines D, Mohseni E, Javadi Y, Mineo C, Vithanage R, Qiu Z, MacLeod C, Pierce G, Gachagan A. Using coded excitation to maintain signal to noise for FMC+TFM on attenuating materials. IEEE. IUS 2019:1–4.
[28] Mamou J, Ketterling JA, Silverman RH. Chirp-coded excitation imaging with a high-frequency ultrasound annular array. Tran. Ult. Feb. 2008;52(2):508–13. https://doi.org/10.1109/TUFFC.2008.670.
[29] Rizwan MK, Laureti S, Mooshofer H, Goldammer M, Ricci M. Ultrasonic imaging of thick carbon fiber reinforced polymers through pulse-compression-based phased array. Appl Sci 2021;11(4):1–15. https://doi.org/10.3390/app11041508.
[30] Wang N, Yang C, Xu J, Shi W, Huang W, Cui Y, Jian X. An improved chirp coded excitation based on compression pulse weighting method in endoscopic ultrasound imaging. IEEE Trans. Ultrason. Ferroelect. Freq. Control 2021;68:446–52.
[31] Yang Y, Wang P, Jia Y, Jing L, Shi Y, Sheng H, Jiang Y, Liu R, Xu Y, Li X. Rail fracture monitoring based on ultrasonic-guided wave technology with multivariate coded excitation. Ultrasonics 2024;136:107164.
[32] Misaridis TX, Gammelmark K, Jørgensen CH, Lindberg N, Thomsen AH, Pedersen MH, Jensen JA. Potential of coded excitation in medical ultrasound imaging. Ultrasonics 2000;38:183–9.
[33] BSI Standards Publication. Non-destructive testing – characterisation and verification of ultrasonic phased array equipment. BS EN ISO; Sep. 2017. p. 18563. 2:2017.
[34] Verasonics. Vantage product specification. May 2022. p. 1–40.
[35] Verasonics "vantage sequence programming manual,". Nov. 2022. p. 1–195.
[36] Drinkwater BW, Wilcox PD. Ultrasonic arrays for non-destructive evaluation: a review. NDT E Int 2006;39(7):525–41.
[37] Nowicki A, Secomski W, Trots I, Litniewski J. Extending penetration depth using coded ultrasonography. Bull. Pol. Acad. Sci. 2004;52(3):215–20.
[38] Hamilton F, Hoskins P, Corner G, Huang Z. Nonlinear harmonic distortion of complementary Golay codes. Ultr. Imag. 2023;45(1):22–9. https://doi.org/10.1177/01617346221147820.
[39] Holmes C, Drinkwater BW, Wilcox PD. Post-processing of the full matrix of ultrasonic transmit–receive array data for non-destructive evaluation. NDT & E. Apr. 2005;38:701–11. https://doi.org/10.1016/j.ndteint.2005.04.002.
[40] Wilcox Paul. MFMC format. 2: [Available from: https://github.com/ndtatbristol/mfmc; 2019.
[41] Lines D. The application of real-time medical ultrasound imaging to NDT. The British institute of NDT annual conference on non-destructive testing for the engineer, keele. September 1983. p. 19–21.
[42] Li C, Pain D, Wilcox PD, Drinkwater BW. Imaging composite material using ultrasonic arrays. NDT Int : independent nondestructive testing and evaluation 2013;53:8–17. https://doi.org/10.1016/j.ndteint.2012.07.006.
[43] Wilcox PD, Jie Z. Quantification of the effect of array element pitch on imaging performance. T-UFFC 2018;65(4):600–16. https://doi.org/10.1109/TUFFC.2018.2794627.
[44] EXTENDE. CIVA NDE software. 2020.
[45] Sweeney NE, et al. In-process phased array ultrasonic weld pool monitoring. NDT E Int 2023;137:102850.
[46] Zhang S, Cheng R, Tao C, Liu X. Appl. Phys. Express 2016;9:047301.
[47] Nicolson E, et al. Dual-tandem phased array Method for Imaging of near-vertical Defects in narrow-gap welds. NDT E Int 2023;135:102808.